PHILOSOPHICAL TRANSACTIONS A

rsta.royalsocietypublishing.org

Research

Cite this article: Ganor Y, Dumitrică T, Feng F, James RD. 2016 Zig-zag twins and helical phase transformations. *Phil. Trans. R. Soc. A* **374**: 20150208.
http://dx.doi.org/10.1098/rsta.2015.0208

Accepted: 1 December 2015

One contribution of 11 to a theme issue 'Trends and challenges in the mechanics of complex materials'.

Subject Areas:
crystal engineering, applied mathematics, microsystems, materials science

Keywords:
martensitic phase transformation, bending, ferromagnetic shape memory, Ni_2MnGa, continuum mechanics

Author for correspondence:
Richard D. James
e-mail: james@umn.edu

Zig-zag twins and helical phase transformations

Yaniv Ganor[1], Traian Dumitrică[2], Fan Feng[1] and Richard D. James[1]

[1]Department of Aerospace Engineering and Mechanics, and [2]Department of Mechanical Engineering, University of Minnesota, Minneapolis, MN 55455, USA

RDJ, 0000-0001-6019-6613

We demonstrate the large bending deformation induced by an array of permanent magnets (applied field ~0.02 T) designed to minimize poles in the bent state of the crystal. Planar cantilevers of NiMnGa (5M modulated martensite) ferromagnetic shape memory alloy deform into an arched shape according to theory, with a zig-zag microstructure that complies with the kinematic and magnetic compatibility between adjacent twin variants. A general theory of bent and twisted states is given, applicable to both twinning and austenite/martensite transformations. Some of these configurations achieve order-of-magnitude amplification of rotation and axial strain. We investigate also atomistic analogues of these bent and twisted configurations with perfect interfaces between phases. These mechanisms of large deformation, induced by small magnetic fields or temperature changes, have potential application to the development of new actuation technologies for micro-robotic systems.

1. Introduction

Martensitic transformations are solid-to-solid phase transformations observed in various crystalline solids. The transformation is characterized by a first-order or discontinuous change in the crystal lattice and the absence of diffusion or reordering of atoms. This transformation is responsible for phenomena of significant scientific interest, including the shape memory effect, the ferromagnetic shape memory effect, magnetic or electric field-induced phase transformation, and a wide variety of phenomena that arise due to the generic sensitivity of magnetoelectric and transport properties to lattice parameters [1], which generally

THE ROYAL SOCIETY PUBLISHING

undergo abrupt changes at transformation. Potential or demonstrated technological applications of these transformation phenomena include solid-state refrigeration [2,3], direct conversion of heat to electricity [4,5], robotics [6], information storage [7], smart windows [8], sensors and actuators [9,10].

Typically, the lattice of the high-temperature phase, austenite, has greater symmetry than that of the low-temperature phase, martensite. This gives rise to variants of martensite—identical crystal lattices of martensite which are obtained by using different deformations of the austenite lattice. The variants rearrange themselves compatibly in a coarse or fine-scale microstructure in order to satisfy imposed boundary conditions.

During the development of the geometrically nonlinear theory of martensitic phase transformations, one of the simplest possible energy-minimizing structures (under free boundary conditions) was constructed theoretically by jumping back and forth between states on the energy wells associated with two variants of martensite, always jumping from one state to a compatible state [11, p. 444]. This microstructure could be realized in a beam. It is of particular practical interest in that the tensile side of the beam experiences the maximum uniaxial stretching possible (among zero-energy microstructures) in this material, while the compressive side has the maximum possible local shrinkage. Thus, the amount of bending is believed to be the largest achievable in a given martensitic material and therefore provides an interesting actuation mechanism (cf. [12,13]). An attempt was made to produce this microstructure by bending a suitably oriented single crystal of Cu-14.0mass%Al-3.5mass%Ni in a pure bending machine [14]. Despite this being a zero-energy microstructure, this experiment was not successful, probably due to metastability phenomena more recently discussed by Ball, Chu and James [15–17], Ball *et al*. [18] and especially Seiner *et al*. [19]. Thus, this simple, natural and interesting energy-minimizing structure has not to our knowledge been observed. Magnetism offers a new handle on the manipulation of microstructure and the lowering of energy barriers. Here, we manipulate magnetic energies to produce this microstructure in the NiMnGa (5M) ferromagnetic shape memory alloy. We demonstrate the formation of these large deflections in an NiMnGa alloy driven by a small magnetic field of 0.02 T. The use of related mechanisms for remotely energized microscale propulsion is discussed in the literature [20].

Motivated by these results, we also update the theory. Seen from a different perspective, the zig-zag bending microstructure can be viewed as an example of an 'objective structure' ([21] and §5) at continuum level, or, more precisely, the transformation of one objective structure to another. This generalizes the zig-zag structure to a large variety of zero-energy microstructures. We develop this idea in the context of martensitic phase transformations in §§3 and 4. As an application of the theory, using the helical group, we find families of zero-energy austenite/martensite structures. Overall, these results show how phase transformations can be used in diverse ways to produce large bending and twisting of extended structures.

Notation and method of visualization. $\mathrm{SO}(3) = \{\mathbf{R} \in \mathbb{R}^{3\times 3} : \mathbf{R}^{\mathrm{T}}\mathbf{R} = \mathbf{I},\ \det \mathbf{R} = +1\}$ denotes rotation matrices, and the notation $\mathbf{a} \otimes \mathbf{n}$ stands for the rank-one tensor constructed from $\mathbf{a}$ and $\mathbf{n}$: in Cartesian components $(\mathbf{a} \otimes \mathbf{n})_{ij} = a_i n_j$. All theoretical pictures of microstructures (at continuum level) shown in this paper are plotted using the following algorithm. (*a*) A deformation $\mathbf{y}(\mathbf{x})$ defined on a domain Ω and having the given values of $\nabla\mathbf{y}$ is constructed analytically. (*b*) Suitable rectangular arrays of points $\mathbf{x}_1, \mathbf{x}_2, \ldots$ are specified on $\partial\Omega$. (*c*) Dots at the points $\mathbf{y}(\mathbf{x}_1), \mathbf{y}(\mathbf{x}_2), \ldots$ are plotted, coloured by their phase or variant. If a magnetization $\mathbf{m}_0 = \mathbf{m}(\mathbf{y}(\mathbf{x}_0))$ is present, corresponding to the deformation gradient $\nabla\mathbf{y}(\mathbf{x}_0)$, then the vector $\mathbf{m}_0$ is plotted in the deformed configuration at $\mathbf{y}(\mathbf{x}_0)$. (The point $\mathbf{x}_0$ is chosen conveniently.) This is a visualization based on a direct interpretation of the Cauchy–Born rule [22] generalized to the magnetic case [23].

2. Magnetoelastic zig-zag twins

The NiMnGa alloy chosen is an off-stoichiometric Heusler alloy with an $L2_1$ cubic structure of the austenite. It undergoes a ferromagnetic transition above room temperature and

a cubic-to-tetragonal martensitic transformation below room temperature. The martensitic transformation is accompanied by a shortening of the cubic unit cell in the [100] direction, and the corresponding easy axis of magnetization is in that direction.

All the bending and twisting deformations constructed in this paper would be poorly represented in geometrically linear theory because of the large rotations involved [24]. A suitable geometrically nonlinear theory of magnetoelasticity, building on the work of Brown [25] but including phase transformation, has been given in [23]. This theory is based on an energy of the form

$$\int_\Omega W(\nabla \mathbf{y}(\mathbf{x}), \mathbf{m}(\mathbf{y}(\mathbf{x})), \theta) - \mathbf{h}_0 \cdot \mathbf{m}(\mathbf{y}(\mathbf{x}))(\det \nabla \mathbf{y}(\mathbf{x}))\, \mathrm{d}\mathbf{x} + \frac{1}{2\gamma} \int_{\mathbb{R}^3} |\nabla \varphi|^2 \, \mathrm{d}\mathbf{y}. \tag{2.1}$$

Here Ω is the reference configuration, which is chosen to represent undistorted austenite at the transformation temperature θ_0, W is the local free-energy density which includes both strain energy and magnetic anisotropy energy, θ is the temperature, $\mathbf{y} : \Omega \to \mathbb{R}^3$ represents the deformation, the vector field $\mathbf{m}(\mathbf{y})$ is the magnetization (defined on the deformed configuration $\mathbf{y}(\Omega)$), $\mathbf{h}_0$ is the applied field and $\gamma = 4\pi$ (cgs units). The last term is the magnetostatic energy: it is evaluated by assigning the magnetization $\mathbf{m}(\mathbf{y})$ and then solving the magnetostatic equation

$$\mathrm{div}(-\nabla \varphi + \mathbf{m}) = 0 \tag{2.2}$$

on all of space, and then inserting the solution $\nabla \varphi$ into the last term of (2.1). There is no ambiguity because (2.2) has a unique solution φ up to an additive constant, among potentials with finite magnetostatic energy.

The key point for this paper is the precise form of the energy wells of W. These are pairs $(\mathbf{F}, \mathbf{m})$ consisting of a 3×3 deformation gradient $\mathbf{F}$ and corresponding magnetization $\mathbf{m}$ that minimize the local free-energy density W. In the case that the martensite is ferromagnetic and $\theta < \theta_0$, these have the following general form [23]:

$$(\mathbf{R}\mathbf{U}_1, \pm \mathbf{R}\mathbf{m}_1),\ (\mathbf{R}\mathbf{U}_2, \pm \mathbf{R}\mathbf{m}_2), \ldots, (\mathbf{R}\mathbf{U}_n, \pm \mathbf{R}\mathbf{m}_n), \quad \mathbf{R} \in \mathrm{SO}(3). \tag{2.3}$$

Note for later use the rotational invariance, and the important fact that the same rotation matrix appears in front of $\mathbf{U}_i$ and $\mathbf{m}_i$. The symmetric, positive-definite tensors $\mathbf{U}_1, \ldots, \mathbf{U}_n$, called transformation stretch tensors, define the *variants* of martensite. All of the wells can be obtained from the first one by using the point group $\mathcal{P} = \{\mathbf{Q}_1, \ldots, \mathbf{Q}_m\}$ of undistorted austenite:

$$\{(\mathbf{U}_1, \mathbf{m}_1), \ldots, (\mathbf{U}_n, \mathbf{m}_n)\} = \{(\mathbf{Q}_i \mathbf{U}_1 \mathbf{Q}_i^{\mathrm{T}}, \mathbf{Q}_i \mathbf{m}_1) : i = 1, \ldots, m\}. \tag{2.4}$$

Generally, $n \leq m$ because there can be degeneracy, as in the tetragonal case below. There can also be a further degeneracy (consistent with (2.4)) in which several magnetizations are paired with the same stretch tensor. (A practical example occurs in the tetragonal phase of Fe_7Pd_3 [26].) We will assume that $W = 0$ on the states given in (2.3) and is positive elsewhere, for $\theta < \theta_0$.

At the transformation temperature, $\theta = \theta_0$, there are one or more additional wells associated with the austenite. If the austenite is ferromagnetic, these are of the form

$$(\mathbf{R}, \pm \mathbf{R}\hat{\mathbf{m}}_1), \ldots (\mathbf{R}, \pm \mathbf{R}\hat{\mathbf{m}}_p), \quad \mathbf{R} \in \mathrm{SO}(3) \text{ and } \{\hat{\mathbf{m}}_1, \ldots, \hat{\mathbf{m}}_p\} = \{\mathbf{Q}_i \hat{\mathbf{m}}_1,\ i = 1, \ldots, m\}. \tag{2.5}$$

If it is non-ferromagnetic the austenite well is simply $(\mathrm{SO}(3), 0)$. Note that in all cases the wells of austenite and martensite are consistent with the same invariance: the transformation $(\mathbf{U}, \mathbf{m}) \to (\mathbf{R}\mathbf{Q}_i \mathbf{U} \mathbf{Q}_i^{\mathrm{T}}, \pm \mathbf{R}\mathbf{Q}_i \mathbf{m})$ takes the wells to themselves for $\mathbf{R} \in \mathrm{SO}(3)$ and $\mathbf{Q}_i$ in the point group of austenite. The austenite well persists as a minimizer of W for $\theta > \theta_0$, but the martensite wells have a higher energy density at these temperatures.

We will make use of a theorem given in [27]: assume two variants of martensite are compatible and the solution for the compatible interface is a type I or type II twin. See [28,29] for the precise definition: in the simplest case type I twins exhibit 180° symmetry of the crystal structure about the normal, while type II twins exhibit 180° symmetry about a vector in the twin plane. In either case, this interface can be made pole-free by the choice of $\pm$, i.e. the condition $\mathrm{div}\, \mathbf{m} = 0$ is satisfied in the weak sense in a neighbourhood of the interface. In view of (2.2), the jump of magnetization at the interface therefore makes no contribution to the magnetostatic energy. Mathematically, this

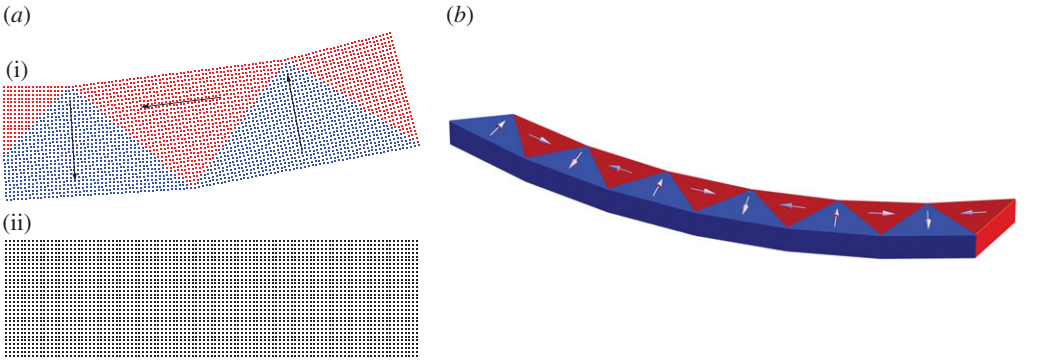

Figure 1. Predicted two-variant microstructure viewed down the [001] axis (*a*) and a three-dimensional view (*b*). Figures drawn with $\eta_1 = 1.013$, $\eta_2 = 0.952$. Note the precise absence of poles on the internal interfaces in the deformed configuration. (*a*) Reference (ii), deformed (i) and (*b*) three-dimensional view with magnetization. (Online version in colour.)

theorem says that if the energy wells have the structure given above and $\mathbf{R} \in \mathrm{SO}(3)$ and vectors $\mathbf{a}, \mathbf{n}$ are chosen to satisfy (for fixed i, j)

$$\mathbf{R}\mathbf{U}_i - \mathbf{U}_j = \mathbf{a} \otimes \mathbf{n}, \tag{2.6}$$

where $\mathbf{U}_i = \mathbf{Q}\mathbf{U}_i\mathbf{Q}^{\mathrm{T}}$ for a suitable twofold orthogonal transformation $\mathbf{Q} \in \mathcal{P}$ (so the two solutions $\mathbf{R}_{\mathrm{I}}, \mathbf{a}_{\mathrm{I}} \otimes \mathbf{n}_{\mathrm{I}}$ and $\mathbf{R}_{\mathrm{II}}, \mathbf{a}_{\mathrm{II}} \otimes \mathbf{n}_{\mathrm{II}}$ of (2.6) are type I/II twins), there is a choice of $\pm$ such that

$$(\mathbf{R}\mathbf{m}_i \pm \mathbf{m}_j) \cdot \hat{\mathbf{n}} = 0, \tag{2.7}$$

where $\hat{\mathbf{n}} = \mathbf{U}_i^{-\mathrm{T}}\mathbf{n}$ is a normal to the interface in the deformed configuration. The key point is that the rotation $\mathbf{R}$ is the same in both (2.6) and (2.7), and therefore the states $(\mathbf{R}\mathbf{U}_i, \mathbf{R}\mathbf{m}_i)$ and $(\mathbf{U}_j, \pm\mathbf{m}_j)$ are on the energy wells. In the case relevant to the experiment reported here, this result is illustrated by figure 1, where it can be seen that the deformed interfaces are compatible and exactly pole-free, despite the distortion, and the local free energy is zero.

The constructions given below consist of piecewise constant magnetization with interfaces satisfying these conditions, and the $\pm$ can be chosen consistently so that all internal interfaces are pole-free. Therefore, the only contribution to the magnetostatic energy is from jumps of the magnetization at the boundary of the body. We noticed that by choosing a suitably oriented, rectangular, single-crystal bar (figure 1) we could make all lateral surfaces of the bar pole-free, except one surface, the convex (blue) surface shown in figure 1*b* having perpendicular magnetization.

Our strategy for an experimental design was to try to remove these remaining poles, thereby lowering the energy. (Fully removing these poles, everything else being the same, would theoretically give zero energy.) A way to fully remove these poles would be to insert magnetic material of the same saturation magnetization outside the bar, with a slightly distorted version of the classical four-domain pattern seen in (100) single-crystal iron [30], so as to create a zero-divergence flux path that simultaneously removes the poles in two neighbouring regions of the same variant. This was considered not practical because the bar deforms, and it is known that the magnetostatic energy is sensitive to small gaps. Alternatively, to achieve a similar reduction of magnetostatic energy, we designed an array of permanent magnets to make a similar circuit, as shown below. Note that the spacing and alternating polarity are matched to the domain structure. Also, ideally, permanent magnets have a fixed magnetization and therefore do not change their own anisotropy energy as the magnetic field in and around them changes.

The alloy chosen for the experimental study undergoes a cubic to tetragonal transformation at macroscopic level with (100) magnetization. The energy-well structure has been determined

previously [31] and is given in the orthonormal cubic basis by

$$\left.\begin{aligned} &\mathbf{U}_1=\begin{pmatrix}\eta_2&0&0\\0&\eta_1&0\\0&0&\eta_1\end{pmatrix},\quad \mathbf{U}_2=\begin{pmatrix}\eta_1&0&0\\0&\eta_2&0\\0&0&\eta_1\end{pmatrix},\quad \mathbf{U}_3=\begin{pmatrix}\eta_1&0&0\\0&\eta_1&0\\0&0&\eta_2\end{pmatrix}\\ &\text{and}\qquad \mathbf{m}_1=m_s(1,0,0)\quad \mathbf{m}_2=m_s(0,1,0)\quad \mathbf{m}_3=m_s(0,0,1),\end{aligned}\right\} \tag{2.8}$$

with $\eta_1=a/a_0=1.013$, $\eta_2=c/a_0=0.952$ and $m_s=600\,\text{emu}\,\text{cm}^{-3}$. We consider variants 1 and 2 only and look for solutions of the equation

$$\mathbf{R}\mathbf{U}_2-\mathbf{U}_1=\mathbf{a}\otimes\mathbf{n},\quad \mathbf{R}\in\text{SO}(3),\ \mathbf{a}\in\mathbb{R}^3,\ \mathbf{n}\in\mathbb{R}^3. \tag{2.9}$$

In fact, in the present case there are precisely two solutions $(\mathbf{R}_1,\mathbf{a}_1\otimes\mathbf{n}_1)$ and $(\mathbf{R}_2,\mathbf{a}_2\otimes\mathbf{n}_2)$ of (2.9), the twins are compound, i.e. there are two different twofold rotations relating the variants as above, and each solution can be considered of both types I and II. (See [28,29] and above.) In the cubic basis in which the distortion matrices are written, the solutions are:

$$\mathbf{R}_1=\frac{1}{\eta_2^2+\eta_1^2}\begin{pmatrix}2\eta_1\eta_2&\eta_1^2-\eta_2^2&0\\ \eta_2^2-\eta_1^2&2\eta_1\eta_2&0\\0&0&\eta_1^2+\eta_2^2\end{pmatrix},\quad \mathbf{a}_1=\frac{\sqrt{2}(\eta_2^2-\eta_1^2)}{\eta_2^2+\eta_1^2}[-\eta_2,\eta_1,0],\quad \mathbf{n}_1=\frac{1}{\sqrt{2}}(1,1,0),$$

$$\mathbf{R}_2=\frac{1}{\eta_2^2+\eta_1^2}\begin{pmatrix}2\eta_1\eta_2&\eta_2^2-\eta_1^2&0\\ \eta_1^2-\eta_2^2&2\eta_1\eta_2&0\\0&0&\eta_1^2+\eta_2^2\end{pmatrix},\quad \mathbf{a}_2=\frac{\sqrt{2}(\eta_1^2-\eta_2^2)}{\eta_2^2+\eta_1^2}[\eta_2,\eta_1,0],\quad \mathbf{n}_2=\frac{1}{\sqrt{2}}(1,-1,0).$$

Note that $\mathbf{R}_1^{\mathrm{T}}=\mathbf{R}_2$.

Now notice the following. By successive premultiplication by powers of $\mathbf{R}_2$, using alternately the two solutions given above, we have the sequence of identities

$$\begin{aligned}\mathbf{U}_1-\mathbf{R}_2\mathbf{U}_2&=-\mathbf{a}_2\otimes\mathbf{n}_2,\\ \mathbf{R}_2\mathbf{U}_2-\mathbf{R}_2^2\mathbf{U}_1&=\mathbf{R}_2^2\mathbf{a}_1\otimes\mathbf{n}_1,\\ \mathbf{R}_2^2\mathbf{U}_1-\mathbf{R}_2^3\mathbf{U}_2&=-\mathbf{R}_2^2\mathbf{a}_2\otimes\mathbf{n}_2,\\ \mathbf{R}_2^3\mathbf{U}_2-\mathbf{R}_2^4\mathbf{U}_1&=\mathbf{R}_2^4\mathbf{a}_1\otimes\mathbf{n}_1,\\ \mathbf{R}_2^4\mathbf{U}_1-\mathbf{R}_2^5\mathbf{U}_2&=-\mathbf{R}_2^4\mathbf{a}_2\otimes\mathbf{n}_2,\ \text{etc.}\end{aligned}$$

This can be thought of as zig-zagging back and forth between the energy wells (figure 2), using the two rank-one connections. The kinematic jump conditions for alternating the deformation gradients

$$\nabla\mathbf{y}=\mathbf{U}_1,\mathbf{R}_2\mathbf{U}_2,\mathbf{R}_2^2\mathbf{U}_1,\mathbf{R}_2^3\mathbf{U}_2,\mathbf{R}_2^4\mathbf{U}_1,\ldots \tag{2.10}$$

across interfaces with normals $\mathbf{n}_2,\mathbf{n}_1,\mathbf{n}_2,\mathbf{n}_1,\mathbf{n}_2,\ldots$ are satisfied, and therefore the associated deformation describes a compatible microstructure, i.e. there is a continuous deformation $\mathbf{y}:\Omega\to\mathbb{R}^3$ satisfying (2.10). Since the powers of the rotation matrix $\mathbf{R}_2$ build up fast, one can expect this deformation to exhibit a lot of bending. Or, from a more mechanical perspective, the tensile side of the beam is parallel to the direction of greatest stretching, while the compressive side of the beam is parallel to the direction of greatest local shrinkage in this alloy.

An explicit form of the deformation, in the case that Ω is a rectangular solid of undistorted austenite with {100} faces and having dimensions $\ell\times w\times h$, is obtained by integrating (2.10) to

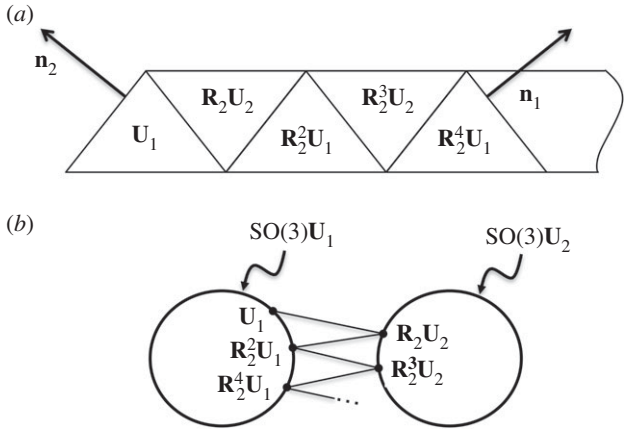

Figure 2. (*a*) Alternating variants in the reference configuration. (*b*) Schematic picture of the energy wells (excluding magnetism). The circles represent SO(3)$\mathbf{U}_1$ and SO(3)$\mathbf{U}_2$, and lines connecting deformation gradients indicate that they differ by a matrix of rank one.

yield the formula

$$\mathbf{y}(\mathbf{x}) = \begin{cases} \mathbf{R}_2^{i+1}\mathbf{U}_1\mathbf{x} + \dfrac{2w}{\sqrt{2}}\displaystyle\sum_{k=1}^{(i-1)/2} k\mathbf{R}_2^{2k}(\mathbf{a}_1 - \mathbf{a}_2) \\ \quad + \dfrac{(i+1)w}{\sqrt{2}}\mathbf{R}_2^{i+1}\mathbf{a}_1, & i = \left[\dfrac{1}{\sqrt{2}w}(\mathbf{x}\cdot\mathbf{n}_1)\right] + \left[\dfrac{1}{\sqrt{2}w}(\mathbf{x}\cdot\mathbf{n}_2)\right] = \text{odd}, \\ \mathbf{R}_2^{i+1}\mathbf{U}_2\mathbf{x} + \dfrac{2w}{\sqrt{2}}\displaystyle\sum_{k=1}^{i/2} k\mathbf{R}_2^{2k}(\mathbf{a}_1 - \mathbf{a}_2), & i = \left[\dfrac{1}{\sqrt{2}w}(\mathbf{x}\cdot\mathbf{n}_1)\right] + \left[\dfrac{1}{\sqrt{2}w}(\mathbf{x}\cdot\mathbf{n}_2)\right] = \text{even}. \end{cases} \tag{2.11}$$

Here, the notation $[x]$ denotes the greatest integer less than or equal to x. For design purposes, we need the angle between the boundaries of neighbouring blue variants in figure 1*a*. This is, from (2.12),

$$\arccos\frac{(\mathbf{y}(4w,0,0) - \mathbf{y}(2w,0,0))\cdot(\mathbf{y}(0,0,0) - \mathbf{y}(2w,0,0))}{|\mathbf{y}(4w,0,0) - \mathbf{y}(2w,0,0)||\mathbf{y}(0,0,0) - \mathbf{y}(2w,0,0)|} = \arccos\frac{\eta_1^4 - 6\eta_1^2\eta_2^2 + \eta_2^4}{(\eta_1^2 + \eta_2^2)^2}. \tag{2.12}$$

With $\eta_1 = 1.013$, $\eta_2 = 0.952$, this angle is 172.9°. This does not depend on the dimensions ℓ, w, h. The length of the edge of the blue region (figure 1*a*) is $2w\eta_1$.

Oriented single-crystal bars of NiMnGa exhibiting 5M modulated martensite (nominal composition $Ni_{50}Mn_{28}Ga_{22}$) were obtained from Adaptamat Ltd. The experiment was carried out in the martensite phase at 25°C, using a specimen size of size $20 \times 2.5 \times 1$ mm. We note that it is currently accepted that the martensite phase of this alloy is monoclinic [32,33] arising from the weakly monoclinic structure. Here, we designed the device based on tetragonal lattice parameters given in §2. Despite the earlier difficulty in the case without magnetism, in the present case these bent states were quite easy to produce by simply moving the bar through the permanent magnet array. The field of the magnets is measured to be 0.02 T at the near surface of the bar in its deformed configuration. From figure 3, it is seen that, while there appears to be complete detwinning in triangles near the magnets, there is incomplete detwinning in some of the other triangles. These are likely to be modulation twins [33] arising from the weakly monoclinic structure. These can either cross the a–c interfaces (see [32] for this terminology and an analysis) or end there. In both cases, these are low-energy interfaces. Evidently, the field is strong enough to bias every other variant completely, while the alternate triangles retain some of these modulation twins. Nevertheless, there is good quantitative agreement between the measured angles of the

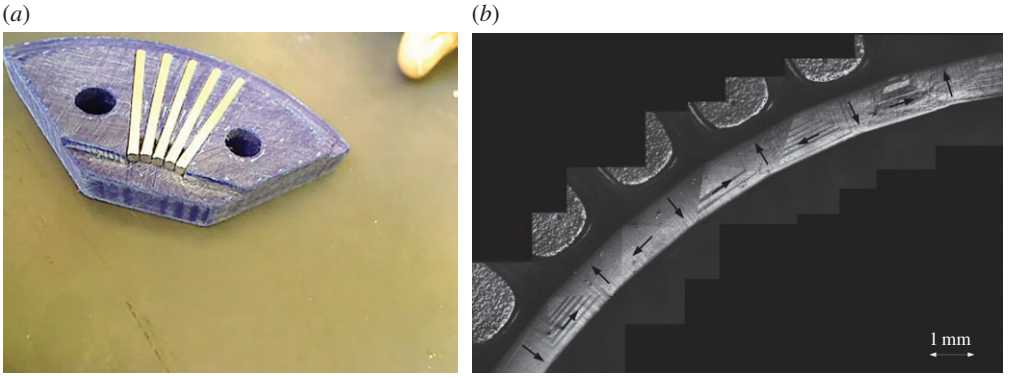

Figure 3. Experimental realization of a two-variant microstructure in NiMnGa. (*a*) The permanent magnet array. Sliding the oriented NiMnGa rod past this array produced the structure seen in (*b*). The magnetization in (*b*) is added by hand. (Online version in colour.)

triangles and the theoretical calculation summarized by figure 1. Evidently, this is due to the fact that the monoclinicity is small.

The bent configuration is quite stable when the field is removed. This can be understood from the fact that, due to the $\pm$ invariance, fine arrays of 180° magnetic domains can be introduced into each triangle, with $1/2$ volume fraction $+$ and $1/2-$ so as to reduce the magnetostatic energy to a low level when no applied field is present.

3. Austenite/martensite circle

As we now explain, the elementary construction given above is a special case of a much more general method of constructing curved zero-energy microstructures. From formula (2.12), one can realize that it is produced by a particular action of two discrete groups of isometries, the group of rotations of multiples of angle θ about a point (circle group) and the one-dimensional translation group. The circle group acts in the deformed configuration, and the one-dimensional translation group acts in the reference configuration. The action of the generator of the circle group (about $\mathbf{y}_0$) is

$$h(\mathbf{y}) = \mathbf{R}_\theta(\mathbf{y} - \mathbf{y}_0) + \mathbf{y}_0. \tag{3.1}$$

The action of the generator of the translation group (translation vector $\mathbf{e}$) is

$$t(\mathbf{x}) = \mathbf{x} + \mathbf{e}. \tag{3.2}$$

Powers of isometries are calculated by composition, $h^k(\mathbf{y}) = h(h(\ldots k\text{−times}\ldots(\mathbf{y}))\ldots) = \mathbf{R}_{k\theta}(\mathbf{y} - \mathbf{y}_0) + \mathbf{y}_0$, $t^k(\mathbf{x}) = t(t(\ldots k\text{−times}\ldots(\mathbf{y}))\ldots) = \mathbf{x} + k\mathbf{e}$. The scheme is the following. Let Ω' be given and consider a zero-energy deformation $\mathbf{y} : \Omega' \to \mathbb{R}^3$ of Ω'. To avoid trivial cases, we suppose that $\Omega' \cap (\Omega' + \mathbf{e})$ is non-empty. Suppose also the following compatibility condition is satisfied on the overlap region $\mathcal{I} = \Omega' \cap (\Omega' + \mathbf{e})$

$$\mathbf{y}(\mathbf{x}) = h(\mathbf{y}(t^{-1}\mathbf{x})) = \mathbf{R}_\theta(\mathbf{y}(\mathbf{x} - \mathbf{e}) - \mathbf{y}_0) + \mathbf{y}_0, \quad \mathbf{x} \in \mathcal{I}. \tag{3.3}$$

In the example above $\mathcal{I}$ is just an interface. Now let the extended reference configuration be $\Omega = \cup_i t^i(\Omega')$. Extend the definition of $\mathbf{y}(\mathbf{x})$ to all of Ω using the formula $\mathbf{y}(\mathbf{x}) = h^i(t^{-i}(\mathbf{x}))$, $\mathbf{x} \in t^i(\Omega')$. It is a simple exercise, using the compatibility condition (3.3) and the group property, that the deformation is consistent on all the overlap regions $t^i(\Omega') \cap t^{i+1}(\Omega')$. The key point is that by differentiation $\nabla\mathbf{y}(t^i(\mathbf{x})) = \mathbf{R}_{i\theta}\nabla\mathbf{y}(\mathbf{x})$. By the frame-indifference of the energy wells, this transformation takes zero-energy states to zero-energy states.

It is an easy exercise to show that, if Ω' consists of two neighbouring triangular solids in a bar of width w, and θ and $\mathbf{e}$ are chosen appropriately, then the deformation $\mathbf{y}(\mathbf{x})$ defined by the formula $\mathbf{y}(\mathbf{x}) = h^i(t^{-i}(\mathbf{x})), \mathbf{x} \in t^i(\Omega')$, agrees precisely with (2.12).

As a second example consider the alloy $Ti_{50}Ni_{40.75}Pd_{9.25}$ [29,34], which undergoes a cubic to orthorhombic phase transformation ($n = 6$). This alloy is not ferromagnetic, so we omit the magnetization, but otherwise the energy wells have the invariance given above. The wells are defined by

$$\left.\begin{aligned} \mathbf{U}_1 &= \begin{pmatrix} \frac{\alpha+\gamma}{2} & \frac{\alpha-\gamma}{2} & 0 \\ \frac{\alpha-\gamma}{2} & \frac{\alpha+\gamma}{2} & 0 \\ 0 & 0 & \beta \end{pmatrix}, \quad \mathbf{U}_2 = \begin{pmatrix} \frac{\alpha+\gamma}{2} & \frac{\gamma-\alpha}{2} & 0 \\ \frac{\gamma-\alpha}{2} & \frac{\alpha+\gamma}{2} & 0 \\ 0 & 0 & \beta \end{pmatrix}, \quad \mathbf{U}_3 = \begin{pmatrix} \frac{\alpha+\gamma}{2} & 0 & \frac{\alpha-\gamma}{2} \\ 0 & \beta & 0 \\ \frac{\alpha-\gamma}{2} & 0 & \frac{\alpha+\gamma}{2} \end{pmatrix}, \\ \mathbf{U}_4 &= \begin{pmatrix} \frac{\alpha+\gamma}{2} & 0 & \frac{\gamma-\alpha}{2} \\ 0 & \beta & 0 \\ \frac{\gamma-\alpha}{2} & 0 & \frac{\alpha+\gamma}{2} \end{pmatrix}, \quad \mathbf{U}_5 = \begin{pmatrix} \beta & 0 & 0 \\ 0 & \frac{\alpha+\gamma}{2} & \frac{\alpha-\gamma}{2} \\ 0 & \frac{\alpha-\gamma}{2} & \frac{\alpha+\gamma}{2} \end{pmatrix}, \quad \mathbf{U}_6 = \begin{pmatrix} \beta & 0 & 0 \\ 0 & \frac{\alpha+\gamma}{2} & \frac{\gamma-\alpha}{2} \\ 0 & \frac{\gamma-\alpha}{2} & \frac{\alpha+\gamma}{2} \end{pmatrix}, \end{aligned}\right\} \tag{3.4}$$

with measured values $\alpha = 1.0000, \beta = 0.9345, \gamma = 1.0645$ (± 0.0002). This particular alloy is interesting in the present context since it was tuned by compositional changes to have $\lambda_2 = \alpha = 1$ where λ_2 is the middle eigenvalue of $\mathbf{U}_1$. (Note that, due to the structure of the energy wells, all $\mathbf{U}_1, \ldots, \mathbf{U}_n$ have the same eigenvalues, which in this case are α, β and γ.) Given $\mathbf{U}_1$ the condition $\lambda_2 = 1$ is necessary and sufficient that the equation

$$\mathbf{R}\mathbf{U}_1 - \mathbf{I} = \mathbf{a} \otimes \mathbf{n} \tag{3.5}$$

has a solution $\mathbf{R} \in \mathrm{SO}(3)$ and $\mathbf{a}, \mathbf{n} \in \mathbb{R}^3$. In fact, if $\lambda_2 = 1$, there are precisely two solutions $(\mathbf{R}_1, \mathbf{a}_1 \otimes \mathbf{n}_1)$ and $(\mathbf{R}_2, \mathbf{a}_2 \otimes \mathbf{n}_2)$ of (3.5). The alloy discussed here,[1] $Ti_{50}Ni_{40.75}Pd_{9.25}$, was preceded by the synthesis of the nearby alloy $Ti_{50}Ni_{39}Pd_{11}$, which also has λ_2 quite close to 1. High-resolution transmission electron microscope (HRTEM) images [35] of $Ti_{50}Ni_{39}Pd_{11}$ revealed many of these 'exact (untwinned) interfaces', and the measured angle in $\mathbf{R}$ and the measured values of $\mathbf{a}$ and $\mathbf{n}$ were shown to agree well with solutions of (3.5).

The existence of the two solutions allows us to construct a deformation similar to that of §2 but using the two solutions of (3.5) and the methods of this section. For this purpose, we choose the first solution $(\mathbf{R}_1, \mathbf{a}_1 \otimes \mathbf{n}_1)$ of (3.5), and we make the particular choices $\mathbf{R}_\theta = \mathbf{R}_1^{\mathrm{T}}$ and, say, $\mathbf{y}_0 = 0$ to specify the group generated by h, and $\mathbf{e} = \omega[1, -1, 0]$ for the group generated by the translation t (ω is chosen conveniently). We also choose a region Ω' consisting of a parallelepiped in the reference configuration bounded by planes of normal $\mathbf{n}_2$ from the second solution a distance $|\mathbf{e}|$ apart. This choice ensures that the overlap condition (3.3) is satisfied. The resulting deformation given by $\mathbf{y}(\mathbf{x}) = h^i(t^{-i}(\mathbf{x})), \mathbf{x} \in t^i(\Omega')$ is shown in figure 4. In this figure, the red triangular regions (austenite) each undergo a pure rigid rotation. The sequence of deformation gradients shown, beginning with the blue triangular region at the end, is $\nabla\mathbf{y} = \mathbf{R}_1\mathbf{U}_1, \mathbf{I}, \mathbf{R}_1^{\mathrm{T}}\mathbf{U}_1, \mathbf{R}_1^{2T}, \mathbf{R}_1^{3T}\mathbf{U}_1, \mathbf{R}_1^{4T}, \mathbf{R}_1^{5T}\mathbf{U}_1, \ldots$.

4. General theory of bent and twisted microstructures

The constructions given above are special cases of a broad class of zero-energy microstructures. The purpose of this section is to define these solutions in the general case and to explain the scope of the method. These solutions have a relation to the theory of objective structures [21] that we explain here. The latter allows us to generalize these solutions to atomic level, where continuum theories such as those based on (2.1) may not be appropriate.

[1]This alloy was found by making $\frac{1}{4}$% changes of composition of Pd [29], starting from the alloy $Ti_{50}Ni_{39}Pd_{11}$, so as to satisfy $\lambda_2 = 1$ to the highest accuracy possible in bulk materials synthesized by arc melting.

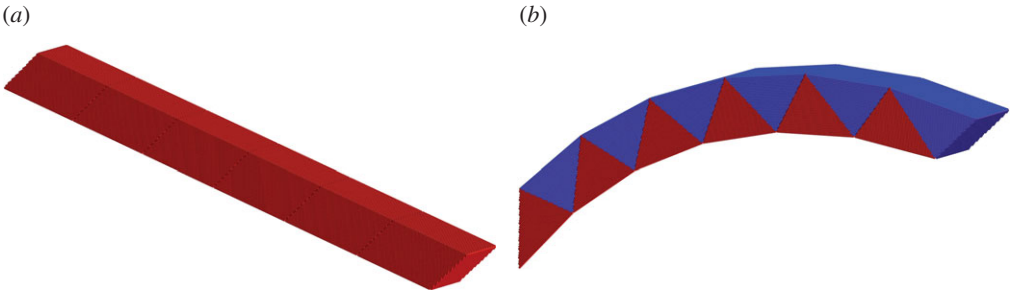

Figure 4. Predicted austenite/single-variant martensite microstructure using measured lattice parameters and the energy-well structure of the alloy $Ti_{50}Ni_{40.75}Pd_{9.25}$. The long direction of the reference configuration is parallel to [1, −1, 0] while its lateral face normals are (1, 1, 0) and (0, 0, 1). (*a*) Reference configuration (austenite) and (*b*) austenite (red), martensite (blue). (Online version in colour.)

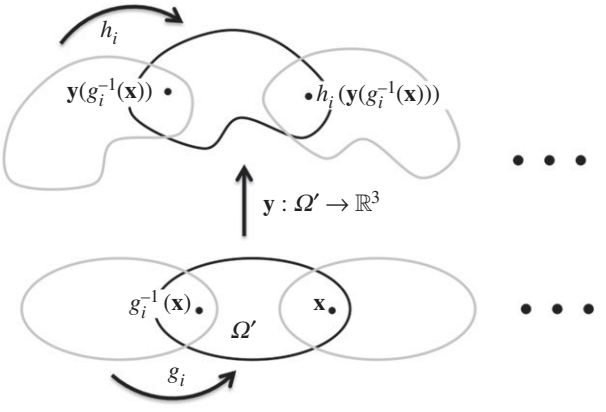

Figure 5. Schematic of the general method of producing compatible bent and twisted microstructures, shown with $r = 1$ and illustrating the consistency condition (4.1).

Isometry groups are groups of orthogonal transformations and translations, with typical elements $(\mathbf{Q}|\mathbf{c})$, $\mathbf{Q} \in \mathrm{O}(3)$ and $\mathbf{c} \in \mathbb{R}^3$, in conventional notation. The multiplication law is $(\mathbf{Q}_1|\mathbf{c}_1)(\mathbf{Q}_2|\mathbf{c}_2) = (\mathbf{Q}_1\mathbf{Q}_2|\mathbf{c}_1 + \mathbf{Q}_1\mathbf{c}_2)$, the identity is $(\mathbf{I}|0)$ and the inverse of $(\mathbf{Q}|\mathbf{c})$ is therefore $(\mathbf{Q}^{\mathrm{T}}| - \mathbf{Q}^{\mathrm{T}}\mathbf{c})$. Under these operations isometries can form groups. The discrete groups of isometries (with the exception of the helical groups) are collected in the *International Tables of Crystallography*, volumes A and E [36,37]. The subperiodic groups [37] are particularly relevant here. The details of the construction of these groups or the nomenclature is not needed here.

We suppose we have two isometry groups, $\mathcal{G}$ and $\mathcal{H}$. As above, $\mathcal{G}$ is associated with the reference configuration and $\mathcal{H}$ to the deformed configuration. For any isometry group, the tensors to the left of the vertical bar in $(\mathbf{Q}|\mathbf{c})$ necessarily form an orthogonal group of tensors which we term the orthogonal part. To ensure that the specification of these groups is consistent with the energy-well structure given in §2, the orthogonal part of $\mathcal{H}$ must be a subgroup of SO(3) (finite or infinite), while the orthogonal part of $\mathcal{G}$ must be a subgroup of the point group of austenite (figure 5).

We suppose also we are given a region Ω' and a deformation $\mathbf{y} : \Omega' \to \mathbb{R}^3$ having a gradient on the wells, $\nabla\mathbf{y}(\mathbf{x}) \in \mathrm{SO}(3) \cup \mathrm{SO}(3)\mathbf{U}_1 \cup \cdots \cup \mathrm{SO}(3)\mathbf{U}_n$. (We comment below on the inclusion of magnetization.) Here we assume that the temperature is at the transformation temperature, $\theta = \theta_0$, so we have included the austenite well. We assume that Ω' and $\mathcal{G}$ have been chosen such that only finitely many members of $g_1, \ldots, g_r \in \mathcal{G}$ have the property $g_i(\Omega') \cap \Omega' \neq \emptyset$ and these

elements commute. To each g_i, $i=1,\dots,r$, we assign a corresponding $h_i, i=1,\dots,r$, in $\mathcal{H}$ such that the $h_1,\dots,h_r$ commute. The $h_1,\dots,h_r$ need not be distinct. Each g_i gives rise to a region $g_i(\Omega')$ that overlaps Ω'. We assume on these overlap regions that the deformation is consistent, in the sense that

$$\mathbf{y}(\mathbf{x}) = h_i(\mathbf{y}(g_i^{-1}\mathbf{x})), \quad \mathbf{x}\in g_i(\Omega'), \quad i=1,\dots,r. \tag{4.1}$$

We denote the Abelian subgroup of $\mathcal{G}$ generated by $g_1,\dots,g_r$ by $\mathcal{G}'$, and similarly let $\mathcal{H}'$ be generated by $h_1,\dots h_r$. We extend Ω' to $\Omega = \cup_{g\in\mathcal{G}'} g(\Omega')$ and correspondingly extend the deformation by the rule

$$\mathbf{y}(\mathbf{x}) = h_1^i\cdots h_r^k(\mathbf{y}((g_1^i\cdots g_r^k)^{-1}\mathbf{x})), \quad \mathbf{x}\in g_1^i\cdots g_r^k(\Omega'). \tag{4.2}$$

Note that the powers are matched. This formula defines a consistent deformation on all of Ω. For example, if $\mathbf{y}$ is continuous on Ω', the extended function defined by (4.2) is continuous on all of Ω. To see this consistency, let $g=g_1^p,\dots,g_r^q$ and $\hat{g}=g_1^{\hat{p}},\dots,g_r^{\hat{q}}$ be such that $g(\Omega')$ and $\hat{g}(\Omega')$ have a non-empty intersection, and define $h=h_1^p,\dots,h_r^q$ and $\hat{h}=h_1^{\hat{p}},\dots,h_r^{\hat{q}}$. Then, the extension (4.2) gives two possible extensions of $\mathbf{y}$. Let $\mathbf{z}\in g(\Omega')\cap\hat{g}(\Omega')$. These two extensions are consistent if

$$h(\mathbf{y}(g^{-1}(\mathbf{z}))) = \hat{h}(\mathbf{y}(\hat{g}^{-1}(\mathbf{z}))). \tag{4.3}$$

Letting $\mathbf{x}=g^{-1}(\mathbf{z})$, (4.3) holds if and only if

$$\mathbf{y}(\mathbf{x}) = h^{-1}\hat{h}(\mathbf{y}((g^{-1}\hat{g})^{-1}(\mathbf{x}))). \tag{4.4}$$

But the latter holds by commutativity and (4.2), because $h^{-1}\hat{h}=h_1^{\hat{p}-p},\dots,h_r^{\hat{q}-q}$ and $g^{-1}\hat{g}=g_1^{\hat{p}-p},\dots,g_r^{\hat{q}-q}$ have the same powers. The choices of the two groups $\mathcal{G}$ and $\mathcal{H}$ above ensure that a zero free-energy deformation of Ω' extends to a zero free-energy deformation of Ω.

As an example, we consider again the alloy $Ti_{50}Ni_{40.75}Pd_{9.25}$ but now choose helical groups for $\mathcal{G}$ and $\mathcal{H}$. In each case, these groups will be generated by a single element so that commutativity is automatically satisfied. The austenite in this alloy is B2-cubic (space group $Pm\bar{3}m$), with Pd substituting for Ni on one of the B2 sublattices, so the natural choice for the orthogonal part of $\mathcal{G}$ is a subgroup of the cubic point group of $Pm\bar{3}m$: we choose an isometry whose orthogonal part is generated by a fourfold rotation about the vertical $\mathbf{e}=[001]$ axis, generated by $g=(\mathbf{R}_{\pi/2}|\mathbf{c}_g)$. We then choose Ω' to be a curved bar bounded by two planes: one is $\mathcal{P}$ and the other is $g^{-1}(\mathcal{P})$. Using the notation following (3.5), $\mathcal{P}$ is chosen to have normal $\mathbf{n}_2$. The material between the planes is divided by the second compatible interface with normal $\mathbf{n}_1$. We assign $\nabla\mathbf{y}=\mathbf{I},\mathbf{R}_1\mathbf{U}_1$ on Ω'. The choice of $\mathcal{P}$ with normal $\mathbf{n}_2$ then ensures the linear term in the overlap condition is satisfied if we choose $h=(\mathbf{Q}|\mathbf{c}_h)$ where $\mathbf{Q}\mathbf{R}_{-\pi/2}-\mathbf{R}_1\mathbf{U}_1=\tilde{\mathbf{a}}\otimes\mathbf{n}_2$. The constant term in the overlap condition then becomes an algebraic relation for $\mathbf{c}_h$ in terms of $\mathbf{c}_g$. The deformation is then given by

$$\mathbf{y}(\mathbf{x}) = h^i\mathbf{y}(g^{-i}\mathbf{x}), \quad \mathbf{x}\in g^i(\Omega'). \tag{4.5}$$

By differentiation, this deformation gives the following sequence of deformation gradients as we go up the helix:

$$\begin{aligned}\nabla\mathbf{y} &= \mathbf{I},\mathbf{R}_1\mathbf{U}_1,\mathbf{Q}\mathbf{R}_{-\pi/2},\mathbf{Q}\mathbf{R}_1\mathbf{U}_1\mathbf{R}_{-\pi/2},\mathbf{Q}^2\mathbf{R}_{-\pi},\mathbf{Q}^2\mathbf{R}_1\mathbf{U}_1\mathbf{R}_{-\pi},\mathbf{Q}^3\mathbf{R}_{-3\pi/2},\mathbf{Q}^3\mathbf{R}_1\mathbf{U}_1\mathbf{R}_{-3\pi/2}\dots\\ &= \mathbf{I},\mathbf{R}_1\mathbf{U}_1,\mathbf{Q}\mathbf{R}_{-\pi/2},\mathbf{Q}\mathbf{R}_1\mathbf{R}_{-\pi/2}\mathbf{U}_2,\mathbf{Q}^2\mathbf{R}_{-\pi},\mathbf{Q}^2\mathbf{R}_1\mathbf{R}_{-\pi}\mathbf{U}_1,\mathbf{Q}^3\mathbf{R}_{-3\pi/2},\mathbf{Q}^3\mathbf{R}_1\mathbf{R}_{-3\pi/2}\mathbf{U}_2,\dots.\end{aligned} \tag{4.6}$$

Note that we only get two distinct variants of martensite (blue and green in figure 6) instead of the expected four, because $\mathbf{R}_\pi\mathbf{U}_1\mathbf{R}_{-\pi}=\mathbf{U}_1$ and $\mathbf{R}_{3\pi/2}\mathbf{U}_1\mathbf{R}_{-3\pi/2}=\mathbf{R}_{\pi/2}\mathbf{U}_1\mathbf{R}_{-\pi/2}=\mathbf{U}_2$. This is a consequence of the orthorhombic symmetry of the martensite. We remark also that the reference configuration in figure 6*a* is *undistorted* austenite: it is not bent and twisted into this shape but it is cut out of a single crystal. Note from the above that $\mathbf{c}_g$ is assignable. This implies that the pitch of the reference configuration is assignable. These kinds of configurations achieve significant amplification of rotations and strains. A smaller pitch of the reference helix gives rise to larger (negative) axial strains: strains of about -40% are possible with the dimensions of the reference bar and volume fractions shown in figure 6 by choosing $\mathbf{c}_g$ appropriately (using the

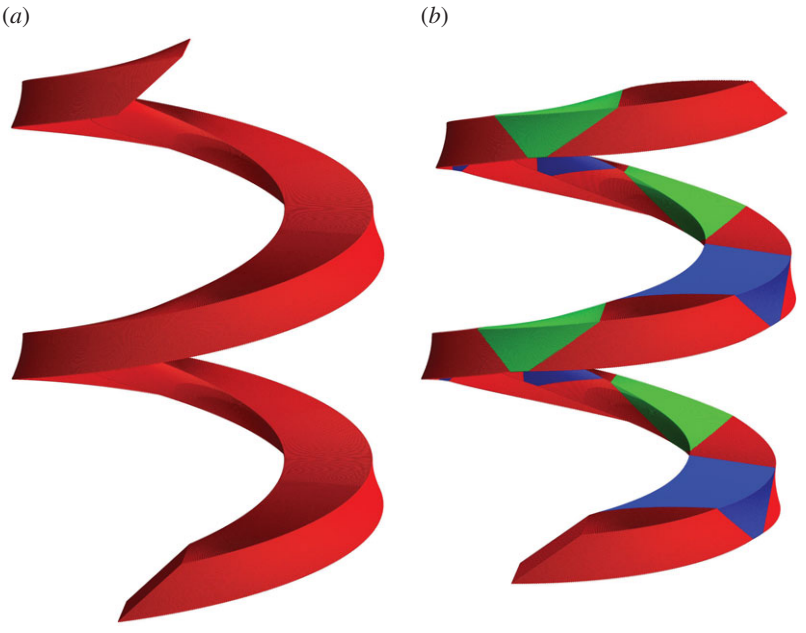

Figure 6. A zero-energy helical microstructure drawn accurately with the lattice parameters of $Ti_{50}Ni_{40.75}Pd_{9.25}$. The reference configuration (*a*) is an unstressed single crystal of austenite that has been cut out in a helical shape. The deformed configuration (*b*) consists of austenite regions (red) and two distinct variants (blue, green) of martensite, all of which are zero free-energy, unstressed states. (*a*) Reference configuration (austenite) and (*b*) austenite (red), martensite (blue, green). (Online version in colour.)

same material). Figure 6 shows an angle of twist of about 45° per turn in transforming from figure 6*a* to figure 6*b*.

5. Bent and twisted microstructures at the atomic level

(a) An atomistic-to-continuum analogy

We remark that the minimum free-energy configurations found above all have direct analogues at the atomic level. This is important as a way to understand the origins of atomic-level behaviour that may differ from continuum-level behaviour as embodied in continuum theories of micromagnetics or phase transformation. The atomistic analogues can be appreciated by noticing that both reference and deformed configurations of all these solutions are 'objective structures' defined in [21]. Objective structures (OSs) are atomic structures which can be divided into disjoint groups of atoms, having a one-to-one correspondence between atoms in any two groups. Equivalently, the atoms can be labelled using the notation (i, j), where i labels the group and j labels the atom within the group. In this notation, all atoms with the same second index are required to be the same species. By definition, to be an OS, every pair of atoms of the form (i, j) and (k, j) are required to see precisely the same atomic environment up to orthogonal transformation. To see that this is true of the structures above, we superimpose the undistorted lattice of austenite on the reference configuration. In fact, the method of visualization used in these figures with a fine array of dots is consistent with the OS definition—we simply ensure that the dots are points of the reference lattice of austenite. Then, following the Cauchy–Born rule [22], we use the calculated zero-energy deformation to transport the atomic positions. This leads to both reference and deformed configurations being perfect objective structures. The basic group of atoms are those contained in Ω'. By definition the reference configuration Ω is the application of the group

$\mathcal{G}$ on Ω', that is, the disjoint groups of atoms are the orbits of the atoms in Ω' under $\mathcal{G}$. This automatically gives an objective structure [38] with the correspondence being that given by the action of $\mathcal{G}$ on Ω'. (That is, suitably oriented observers stationed at $\mathbf{x}$ and $g(\mathbf{x})$ see the same atomic environment, assuming of course that the helix is extended to infinity so there are no ends.) By construction, the deformed configuration is also an objective structure: replace $\mathcal{G}$ by $\mathcal{H}$ and Ω' by $\mathbf{y}(\Omega')$.

The analogy can be pushed one step further, as described in [39,40]. If one sets up a molecular dynamics simulation (with very general classes of atomic forces) for the atoms in $\mathbf{y}(\Omega')$ but determines the image atoms using the group $\mathcal{H}$, just as above, so only the atoms in $\mathbf{y}(\Omega')$ are actually simulated, but forces on these from all the other atoms are accounted for, then it follows that all the atoms satisfy exactly the equations of molecular dynamics. This is a special case of the method of objective molecular dynamics (OMD [39,40]). In fact, a certain time dependence of the group parameter $\mathbf{c}_h$ can be introduced [39], which leads to exact molecular dynamics for every atom, but which also includes a macroscopic motion. For the case shown in figure 6, this method could be used to study stress-induced transformation due to pulling the helix vertically at a constant (assignable) axial strain rate. We note that this analogue between continuum-level free-energy minimizers and exact solutions of the equations of molecular dynamics is sufficiently flexible to allow for phenomena such as surface relaxation in either the continuum or atomistic theory.[2] Using atomic forces appropriate to a transforming material, it would be interesting to set up some computations of this type at small scales. A direct comparison between the results of atomic and continuum theory could then be made.

The analogy between atomic and continuum level is nearly perfect for these solutions, except for one curiosity. That is, the atomic-level solutions of OMD allow all possible discrete groups of isometries, whereas the continuum-level analogue described here requires Abelian groups. Evidently, this is related to the use of deformations in continuum mechanics, and the fact that the associated conditions of compatibility used heavily here are fundamentally related to the Abelian process of getting the same answer by taking different paths to the same point.

(b) Perfect atomistic interfaces

In §4, we used the idea of objective structures to generate energy-minimizing bent and twisted configurations of a material (e.g. $Ti_{50}Ni_{40.75}Pd_{9.25}$) exhibiting perfect interfaces between austenite and single-variant martensite. In §5a, we noticed that the resulting configurations have the same structure as exact solutions of the equations of molecular dynamics generated using the theory of objective structures. For the latter the bent and twisted structure is the orbit under a helical group of the domain $\mathbf{y}(\Omega')$.

Note that the reference configuration plays no direct role in the construction of twisted states at the atomic level. We can simply work with a collection of atoms and an isometry group. The simplest objective structures are the orbits of a single atom position under an isometry group. The examples above raise the question of whether two objective structures, each generated as the orbit of a single atom position, can meet along an interface with perfect matching of atoms across the interface. Here we show by examples that this is the case. In fact, the method of construction here is strictly mathematically analogous to the method used to construct the helical structures shown in figure 6*b*. A complete analysis is given in a forthcoming paper [43].

Helical atomistic structures are surprisingly common. All single-walled carbon nanotubes of all chiralities are given by a helical group acting on a single atomic position. (See [39] for formulae for the helical groups.) They are particularly common in viruses. In [13], it is shown that the positions and orientations of molecules on the tail sheath of bacteriophage T4 are accurately given by a helical group operating on a single molecule. In fact, the tail sheath of this virus actually undergoes a phase transformation during the process of infection, and both phases are orbits

[2]See Salje *et al*. [41] for a review of interfacial relaxation in the context of continuum theory of ferroelectric phase transformations and Diao *et al*. [42] for interesting atomistic effects such as surface energy induced phase transformation in atomistic theory.

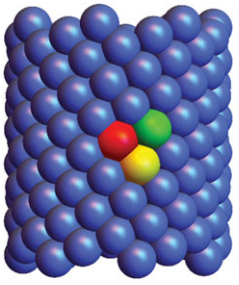

Figure 7. Nearest-neighbour generators: the isometry g_1 maps the red atom to the yellow atom, while the isometry g_2 maps the red atom to the green one. (Online version in colour.)

of the same helical group, but with different parameters. (These parameters do not satisfy the strong conditions of compatibility given below.) As another important example, the Ebola virion apparently exhibits four helical structures, see [44].

Consider two helical groups $\mathcal{G}_a$ and $\mathcal{G}_b$. While many interesting atomic structures can be constructed using powers of a single isometry (as above), this is not suitable for our construction of perfectly matching atomic interfaces. That is because structures constructed from powers of a single isometry typically have nearby atoms (often, nearest neighbours) that are generated by very different powers of the isometry. One can imagine starting at an atom, then going one by one around a long helix to another atom which is near the first one. In such cases, nearby powers of the isometry are not good kinematic indicators of nearby atoms. Fortunately, under very mild assumptions on the group parameters [43], one can always switch to *nearest-neighbour generators* (figure 7). This is a pair of commuting screw transformations g_1 and g_2 such that $g_1^{i+1}g_2^j(\mathbf{x})$ and $g_1^{i-1}g_2^j(\mathbf{x})$ are nearest neighbours of $g_1^i g_2^j(\mathbf{x})$, and $g_1^i g_2^{j+1}(\mathbf{x})$ and $g_1^i g_2^{j-1}(\mathbf{x})$ are second nearest neighbours of $g_1^i g_2^j(\mathbf{x})$, for all $\mathbf{x}\in\mathbb{R}^3$ not on the common screw axis. In that case we can use the powers (i,j) as a surrogate for metric properties. In this framework, the positions of atoms on the helical structures of phases a and b are given by formulae of the type $\mathbf{y}(i,j)=g_1^i g_2^j(\mathbf{r})$, or, explicitly,

$$\left.\begin{aligned}\mathbf{y}_a(i,j)&=\mathbf{Q}^a_{i\psi_a+j\beta_a}\mathbf{r}_a+(im_1^a+jm_2^a)\tau_a\mathbf{e}_a+\mathbf{z}_a,\ i\in\mathbb{Z},\ j=1,\dots,j^\star_a\\ \text{and}\qquad \mathbf{y}_b(i,j)&=\mathbf{Q}^b_{i\psi_b+j\beta_b}\mathbf{r}_b+(im_1^b+jm_2^b)\tau_b\mathbf{e}_b+\mathbf{z}_b,\quad i\in\mathbb{Z},\ j=1,\dots,j^\star_b,\end{aligned}\right\}\tag{5.1}$$

where $\mathbf{Q}^{a,b}_\theta\in\mathrm{SO}(3)$, $\mathbf{Q}^a_\theta\mathbf{e}_a=\mathbf{e}_a$, $\mathbf{Q}^b_\theta\mathbf{e}_b=\mathbf{e}_b$, $\mathbf{r}_a,\mathbf{r}_b\in\mathbb{R}^3$, and the subscript θ denotes the angle: $\operatorname{tr}\mathbf{Q}^{a,b}_\theta=1+2\cos\theta$. The integers $j^\star_{a,b}$ specifying the domain of j come out of the switch to nearest-neighbour generators. In words, the formulae (5.1) give the positions of atoms (i,j) in phases a or b.

The *structural parameters* (i.e. the analogues of the lattice parameters α,β,γ of (3.4)) are constants that determine the structure up to an overall rotation and translation. The structural parameters of the two phases are therefore $\psi_{a,b},\beta_{a,b},\tau_{a,b},r_{a,b}\in\mathbb{R}$; $m_1^{a,b},m_2^{a,b}\in\mathbb{Z}$, where $r_{a,b}=|\mathbf{r}_{a,b}|$.

Having set up this metric kinematics, the simplest way to impose compatibility is to notice that the formulae (5.1) for $\mathbf{y}_a$ and $\mathbf{y}_b$ make perfect sense when i,j are real numbers rather than integers. One can term this smooth extension to $i\in\mathbb{R}$, $0<j<j^\star_{a,b}$, the *canonical interpolation*. Using the canonical interpolation, compatibility can now be imposed in the usual way of continuum mechanics. A smooth interface $\hat{i}(s),\hat{j}(s),s\in(s_1,s_2)$ is given in arclength parametrization, $\hat{i}'(s)^2+\hat{j}'(s)^2=1$ (without loss of generality) and lying in an appropriate domain $1<s_1<s_2<\min\{j^\star_a,j^\star_b\}$. Assuming that $\hat{i}'\neq0$, local deformation of the form

$$\mathbf{y}(i,j)=\begin{cases}\mathbf{y}_a(i,j), & j>\hat{j}(s),\\ \mathbf{y}_b(i,j), & j\le\hat{j}(s),\end{cases}\tag{5.2}$$

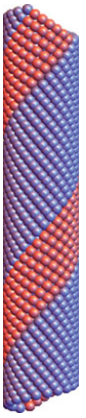

Figure 8. Perfect interface between helical states. See text. (Online version in colour.)

is compatible if there is an amplitude $\mathbf{a}(s)$, $s_1 < s < s_2$ such that

$$[|(\mathbf{y}_{\prime i}, \mathbf{y}_{\prime j})|] = (\mathbf{y}_{a\prime i} - \mathbf{y}_{b\prime i}, \mathbf{y}_{a\prime j} - \mathbf{y}_{b\prime j}) = \mathbf{a}(\hat{i}', -\hat{j}'), \tag{5.3}$$

or, equivalently,

$$[|\mathbf{y}_{\prime i}|]\hat{j}' + [|\mathbf{y}_{\prime j}|]\hat{i}' = 0, \tag{5.4}$$

with $\hat{i}'^2 + \hat{j}'^2 = 1$. A complete solution of (5.4) for all choices of interface and structural parameters is given in forthcoming work [43], so we here just give a typical family of examples. That is the case of $\hat{i} = \text{const.}$ and structural parameters

$$\beta_a = \beta_b \neq 0, \quad \mathbf{r}_b = \mathbf{Q}_{\hat{i}(\psi_a - \psi_b)}\mathbf{r}_a, \quad \mathbf{e}_b = \mathbf{e}_a, \quad \mathbf{Q}^a_\theta = \mathbf{Q}^b_\theta, \quad m^a_1\tau_a = m^b_1\tau_b. \tag{5.5}$$

These conditions can be considered (one subcase of) the atomic-level analogue, for helical structures, of the macroscopic condition $\lambda_2 = 1$ used above. A typical picture of an interface satisfying these conditions is shown in figure 8. It is seen that completion of the phase transformation can occur by widening the red region, so it consumes the whole tube. During this process, significant bending and twisting occurs due to the (small) change of lattice parameters. By appropriately removing red and blue atoms, it is seen that this state is closely analogous to the state shown in figure 6, except here there is only one variant of the blue phase. It remains to be seen whether the concept of 'variant' has any meaning for helical atomistic phases.

6. Summary and discussion

We have demonstrated experimentally large bending due to phase transformation and magnetism. An array of permanent magnets was designed according to a geometrically nonlinear theory of magnetoelastic phase transformations, and these easily induced bending of an oriented single-crystal beam. Since the tensile side of the beam experiences the greatest tensile strain possible in the material, and the compressive side experiences the largest local negative strain, this configuration is believed to produce the largest zero-energy bending curvature possible in a phase-transforming material. The construction is generic and applies to a broad class of transforming materials. Gradual bending from the undeformed to the deformed configurations is possible by spacing the triangles shown in figure 2 further apart. This would require a tunable array of magnets, which could be made with a fine array of patterned coils.

The elimination of internal poles at twin boundaries in this configuration is due to a fundamental relationship between deformation and magnetization that arises from the symmetries of the energy wells. This is also often true of energy wells in a single-crystal ferroelectric [45] to which the analysis then applies. Essentially, ferroelectrics need not exhibit the

± invariance of (2.4), although in many cases this follows necessarily from the other invariances present (frame indifference and point group invariance). Besides the analogue of magnetostatic energy, the total ferroelectric energy also has terms arising from free charges that would have to be considered.

The standard scaling of magnetoelasticity $\mathbf{y}(\mathbf{x}) \to \lambda\mathbf{y}((1/\lambda)\mathbf{x})$, $\mathbf{m}(\mathbf{y}) \to \mathbf{m}((1/\lambda)\mathbf{y})$ preserves the energy wells and sends zero-energy solutions to zero-energy solutions, but multiplies curvatures by a factor $1/\lambda$. Therefore, these solutions have the property that the curvature scales inversely as a linear dimension as they are scaled down in a geometrically similar way. Consider the case of the austenite/martensite structure of figure 4*b*. If the temperature is raised to $\theta > \theta_0$, then this is no longer a zero-energy microstructure. In fact its energy at temperature θ scales as the volume, λ^3, while elastic bending energies scale as λ^5. Thus, there is a strong driving force, forcing it back to the unique (up to rotations and translations) reference configuration, figure 4*b* → 4*a*. For a finer analysis, consider a beam of thickness h, width b and length ℓ in the reference configuration, and the austenite has typical extensional modulus E. We can imagine hanging a vertical weight on the end of the beam in figure 4*b*. The weight F will be lifted substantially by heating the crystal, as the crystal returns to a nearly straight shape, if (i) the energy of raising the weight F is comparable to the free-energy difference between phases at θ and (ii) the weight F is small enough so that it does not cause much ordinary elastic bending of the austenite. The latter requires that $F \ll Ebh^3/12\ell^2$ while the former is $F \sim bh\Delta W$, where $\Delta W = W(\mathbf{I}, \theta) - W(\mathbf{U}_1, \theta)$. (Here, we have neglected ordinary thermal expansion of austenite and martensite.) As in the derivation of the Clausius–Clapeyron equation, we approximate $\Delta W = (\partial W/\partial\theta(\mathbf{I}, \theta_0) - (\partial W/\partial\theta)(\mathbf{U}_1, \theta_0))(\theta - \theta_0) = (\eta(\mathbf{U}_1, \theta_0) - \eta(\mathbf{I}, \theta_0))(\theta - \theta_0) = L(\theta - \theta_0)/\theta_0$, where η is the entropy density and L is the latent heat. This gives the useful regime

$$\frac{\theta - \theta_0}{\theta_0} \ll \frac{E}{12\,L}\left(\frac{h}{\ell}\right)^2 \tag{6.1}$$

(θ in kelvin). Using, for example, typical values for NiTi ($L = (25\,\mathrm{J\,g^{-1}})(6.45\,\mathrm{g\,cm^{-3}}) = 160\,\mathrm{J\,cm^{-3}}$, $E = 80\,\mathrm{GPa}$), we get $(\theta - \theta_0)/\theta_0 \ll 40(h/\ell)^2$. Typical expected temperature excursions of approximately 20 K from a transformation temperature of 300 K are therefore reasonable for a cantilever of aspect ratio $h/\ell = 1/10$. The width b does not enter this comparison, and can be used to increase (or decrease) the force. In the magnetic case, the important magnetic energies—anisotropy, magnetostatic, Zeeman—also scale favourably as the volume.

We have given a general method of zero-energy microstructures that exhibit bending and twisting. These are based on the use of Abelian, discrete groups of isometries. The listing of volume E of the International Tables [37] shows that there are many of these. Also, the helical groups, which are not listed there (due, in our view, to an unfortunate choice of classification scheme), provide additional interesting groups. Thus, systematic study is warranted.

We have also remarked that, based on the Cauchy–Born rule, these solutions have exact analogues at the atomic level, using molecular dynamics with general atomic forces. These are solutions of the equations of motion at the atomic level, but their stability properties might be quite different. This provides an unusual opportunity to understand the behaviour of phase transformations at the atomic level, especially in comparison with more familiar continuum-level behaviour.

Data accessibility. All constructions, figures and data associated with this paper can be reproduced by using the models and equations given explicitly in the paper.

Authors' contributions. Y.G. conceived and carried out the experiment on zig-zag twins; T.D. and R.D.J. participated in the design of the research; F.F. contributed to the design of perfect atomistic interfaces between helical states; R.D.J. drafted the manuscript. All authors approve the final form of the paper.

Competing interests. The authors have no competing interests.

Funding. R.D.J. and F.F. were supported by AFOSR (FA9550-15-1-0207), ONR (N00014-14-0714), NSF/PIRE (OISE-0967140) and the MURI Program (FA9550-12-1-0458). T.D. was supported by the NSF (CMMI-1332228).

References

1. James R, Zhang Z. 2005 A way to search for multiferroic materials with unlikely combinations of physical properties. In *Magnetism and structure in functional materials*, vol. 9 (eds A Planes, L Manõsa, A Saxena), pp. 159–175. Springer Series in Materials Science. Berlin, Germany: Springer.
2. Cui J, Wu Y, Muehlbauer J, Hwang Y, Radermacher R, Fackler S, Wuttig M, Takeuchi I. 2012 Demonstration of high efficiency elastocaloric cooling with large ΔT using NiTi wires. *Appl. Phys. Lett.* **101**, 073904. (doi:10.1063/1.4746257)
3. Liu J, Gottschall T, Skokov KP, Moore JD, Gutfleisch O. 2012 Giant magnetocaloric effect driven by structural transitions. *Nat. Mater.* **11**, 620–626. (doi:10.1038/nmat3334)
4. Song Y, Bhatti K, Srinivasan V, Leighton C, James RD. 2013 Thermodynamics of energy conversion via first order phase transformation in low hysteresis magnetic materials. *Energy Environ. Sci.* **6**, 1315. (doi:10.1039/c3ee24021e)
5. Srivastava KBV, Song Y, James RD. 2011 The direct conversion of heat to electricity using multiferroic alloys. *Adv. Energy Mater.* **1**, 97–104. (doi:10.1002/aenm.201000048)
6. Farias V, Solis L, Melendez L, Garcia C, Velazquez R. 2009 A four-fingered robot hand with shape memory alloys. In *AFRICON '09, Nairobi, Kenya, 23–25 September 2009*, pp. 1–6. Piscataway, NJ: IEEE.
7. Wuttig M, Yamada N. 2007 Phase-change materials for rewriteable data storage. *Nat. Mater.* **6**, 824–832. (doi:10.1038/nmat2009)
8. Zhou J, Gao Y, Zhang Z, Luo H, Cao C, Chen Z, Dai L, Liu X. 2013 VO_2 thermochromic smart window for energy savings and generation. *Sci. Rep.* **3**, 3029. (doi:10.1038/srep03029)
9. Li MH, Keller P, Li B, Wang X, Brunet M. 2003 Light-driven side-on nematic elastomer actuators. *Adv. Mater.* **15**, 569–572. (doi:10.1002/adma.200304552)
10. Otsuka K, Wayman CM. 1999 *Shape memory materials*. Cambridge, UK: Cambridge University Press.
11. Ball JM, James RD. 1992 Proposed experimental tests of a theory of fine microstructure and the two-well problem. *Phil. Trans. R. Soc. Lond. A* **338**, 389–450. (doi:10.1098/rsta.1992.0013)
12. Bhattacharya K, James RD. 2005 The material is the machine. *Science* **307**, 53–54. (doi:10.1126/science.1100892)
13. Falk W, James RD. 2006 Elasticity theory for self-assembled protein lattices with application to the martensitic phase transition in bacteriophage T4 tail sheath. *Phys. Rev. E* **73**, 011917. (doi:10.1103/PhysRevE.73.011917)
14. Berg B. 1993 Bending of superelastic wires. PhD thesis, University of Minnesota, Department of Aerospace Engineering and Mechanics, Minneapolis, MN, USA.
15. Ball J, Chu C, James R. 1995 Hysteresis during stress-induced variant rearrangement. *J. Phys. IV* **C8**, 245–251. (doi:10.1051/jp4:1995834)
16. Ball J, James R. 1996 Local minimizers and phase transformations. *Z. Angew. Math. Mech.* **76**, 389–392.
17. Ball JM, James RD. 2015 Incompatible sets of gradients and metastability. *Arch. Ration. Mech. Anal.* **218**, 1363–1416. (doi:10.1007/s00205-015-0883-9)
18. Ball JM, Koumatos K, Seiner H. 2012 Nucleation of austenite in mechanically stabilized martensite by localized heating. *J. Alloys Comp.* **577**, S37–S42. (doi:10.1016/j.jallcom.2011.11.070)
19. Seiner H, Straka L, Heczko O. 2014 A microstructural model of motion of macro-twin interfaces in Ni–Mn–Ga 10 m martensite. *J. Mech. Phys. Solids* **64**, 198–211. (doi:10.1016/j.jmps.2013.11.004)
20. Kanner OY, Shilo D, Sheng J, James RD, Ganor Y. 2013 Ferromagnetic shape memory flapper for remotely actuated propulsion systems. *Smart Mater. Struct.* **22**, 085030. (doi:10.1088/0964-1726/22/8/085030)
21. James RD. 2006 Objective structures. *J. Mech. Phys. Solids* **54**, 2354–2390. (doi:10.1016/j.jmps.2006.05.008)
22. Ericksen J. 2008 On the Cauchy–Born rule. *Math. Mech. Solids* **13**, 199–220. (doi:10.1177/1081286507086898)

23. James R, Kinderlehrer D. 1993 Theory of magnetostriction with applications to $Tb_xDy_{1-x}Fe_2$. *Phil. Mag. B* **68**, 237–274. (doi:10.1080/01418639308226405)
24. Bhattacharya K. 1993 Comparison of geometrically nonlinear and linear theories of martensitic transformation. *Cont. Mech. Thermodyn.* **5**, 205–242. (doi:10.1007/BF01126525)
25. Brown Jr WF. 1966 *Magnetoelastic interactions*. Springer Tracts in Natural Philosophy Series 9. Berlin, Germany: Springer.
26. Cui J, Shield TW, James RD. 2004 Ferromagnetic shape memory effects in an iron-palladium ferromagnetic shape-memory alloy. *Acta Mater.* **52**, 35–47. (doi:10.1016/j.actamat.2003.08.024)
27. James R, Hane K. 2000 Martensitic transformations and shape memory materials. *Acta Mater.* **48**, 197–222. (doi:10.1016/S1359-6454(99)00295-5)
28. Bhattacharya K. 2003 *Microstructure of martensite*. Oxford, UK: Oxford University Press.
29. Chen X, Song Y, Dabade V, James RD. 2013 Study of the cofactor conditions: conditions of supercompatibility between phases. *J. Mech. Phys. Solids* **61**, 2566–2587. (doi:10.1016/j.jmps.2013.08.004)
30. Williams HJ, Bozorth RM, Shockley W. 1949 Magnetic domain patterns on single crystals of silicon iron. *Phys. Rev.* **75**, 155–178. (doi:10.1103/PhysRev.75.155)
31. Tickle R, James R, Shield T, Wuttig M, Kokorin V. 1999 Ferromagnetic shape memory in the NiMnGa system. *Mag. IEEE Trans.* **35**, 4301–4310. (doi:10.1109/20.799080)
32. Heczko O, Straka L, Seiner H. 2013 Different microstructures of mobile twin boundaries in 10M modulated Ni–Mn–Ga martensite. *Acta Mater.* **61**, 622–631. (doi:10.1016/j.actamat.2012.10.007)
33. Straka L, Heczko O, Seiner H, Lanska N, Drahokoupil J, Soroka A, Fähler S, Hänninen H, Sozinov A. 2011 Highly mobile twinned interface in 10M modulated Ni–Mn–Ga martensite: analysis beyond the tetragonal approximation of lattice. *Acta Mater.* **59**, 7450–7463. (doi:10.1016/j.actamat.2011.09.020)
34. Cui J *et al.* 2006 Combinatorial search of thermoelastic shape memory alloys with extremely small hysteresis width. *Nat. Mater.* **5**, 286–290. (doi:10.1038/nmat1593)
35. Delville R, Kasinathan S, Zhang Z, Humbeeck V, James RD, Schryvers D. 2010 A transmission electron microscopy study of phase compatibility in low hysteresis shape memory alloys. *Phil. Mag.* **90**, 177–195. (doi:10.1080/14786430903074755)
36. Hahn T (ed.). 2002 *International tables for crystallography. Volume A: Space-group symmetry*. Dordrecht, The Netherlands: Kluwer Academic Publishers.
37. Kopsky V, Litvin DB (eds). 2002 *International tables for crystallography. Volume E: Subperiodic groups*. Dordrecht, The Netherlands: Kluwer Academic Publishers.
38. Dayal K, Elliott RS, James RD. In preparation. Objective formulas.
39. Dayal K, James RD. 2010 Nonequilibrium molecular dynamics for bulk materials and nanostructures. *J. Mech. Phys. Solids* **58**, 145–163. (doi:10.1016/j.jmps.2009.10.008)
40. Dumitrică T, James RD. 2007 Objective molecular dynamics. *J. Mech. Phys. Solids* **55**, 2206–2236. (doi:10.1016/j.jmps.2007.03.001)
41. Salje EKH, Hayward SA, Lee WT. 2005 Ferroelastic phase transitions: structure and microstructure. *Acta Crystallogr. Sect. A Found. Crystallogr.* **61**, 3–18. (doi:10.1107/S0108767304020318)
42. Diao J, Gall K, Dunn ML. 2003 Surface-stress-induced phase transformation in metal nanowires. *Nat. Mater.* **2**, 656–660. (doi:10.1107/S0108767304020318)
43. Feng F, James R. In preparation. Phase transformations in objective structures.
44. Konstantinov I, Stefanov Y, Kovalevsky A, Bakulina A. 2016 The Ebloa virus. See https://www.nsf. gov/news/special_reports/scivis/popup/ebola.jsp.
45. Dayal K, Bhattacharya K. 2007 A real-space non-local phase-field model of ferroelectric domain patterns in complex geometries. *Acta Mater.* **55**, 1907–1917. (doi:10.1016/j.actamat.2006.10.049)